International Journal of Imaging Systems and Technology

WILEY

RESEARCH ARTICLE OPEN ACCESS

Automatic Segmentation of the Outer and Inner Foveal Avascular Zone by Convolutional Filters

Carlos Ruiz-Tabuenca[1] | Isabel Pinilla[2,3] | Elvira Orduna-Hospital[1,2] | Francisco Javier Salgado-Remacha[1]

[1]Departamento de Física Aplicada, Universidad de Zaragoza, Zaragoza, Spain | [2]Aragon Institute for Health Research (IIS Aragon), Zaragoza, Spain | [3]Department of Ophthalmology, Lozano Blesa University Hospital, Zaragoza, Spain

Correspondence: Carlos Ruiz-Tabuenca (760104@unizar.es)

Received: 1 April 2025 | **Revised:** 25 September 2025 | **Accepted:** 24 December 2025

Keywords: automatization algorithm | convolution | diabetes mellitus | image processing | statistical analysis

ABSTRACT

In this paper a new algorithm for segmentation of the foveal avascular zone in optical coherence tomography angiography images of the superficial capillary plexus is presented and evaluated. The algorithm is based on convolutional techniques, and for evaluation it has been compared with a collection of manual segmentations. Besides its performance, the main novelty presented is the ability to distinguish the purely avascular zone from the transitional environment whose importance has been recently pointed out. Its capability has been tested on images of patients with different types of diabetes mellitus, obtaining error rates between 1% and 1.5%. In addition, statistical data is shown for the segmented areas (including the transition zone, which had never been studied before) as a function of the type of diabetes. Moreover, a linear trend in outer and inner axis ratios is also observed. Overall, the algorithm represents a new approach in the analysis of optical coherence tomography angiography images, offering clinicians a new and reliable tool for objective foveal avascular zone segmentation of the superficial capillary plexus. Both the code and the dataset used are also made public in the cited repositories.

1 | Introduction

Image acquisition plays a fundamental role in the diagnosis of ocular diseases process. A variety of techniques are employed to capture detailed images of ocular structures, with optical coherence tomography (OCT) standing out as a widely adopted approach. This non-invasive technique provides high-resolution cross-sectional images of internal ocular structures, enabling detailed visualization of retinal layers, including critical areas such as the fovea. In recent years, optical coherence tomography angiography (OCTA) has emerged as a powerful imaging technique that enables the visualization of retinal vascular plexuses without the need for contrast dye injection, allowing for a detailed assessment of microvascular structures and blood flow dynamics in the retina. OCTA has become an essential tool in the diagnosis and monitoring of various retinal and choroidal diseases, offering a safer and more accessible alternative [1].

As OCT scans are three-dimensional, all the images obtained are, in fact, different projections of the scanned volume. Depending on which axis is used to make the projection, the obtained image is classified as A-scan or B-scan. A-scan images consist of transversal retinal planes, and are ideal for visualization of the Foveal Avascular Zone (FAZ) and the surrounding capillaries, while B-scans show in-depth slices of the eye, making them useful for visualization of the different layers that make up the tissues. Both A-scans and B-scans can be retrieved at different depths, obtaining different projection results. In our case, we limited our analysis to A-scan images of the Superficial Capillary Plexus (SCP), so, from now on, all mention to any OCT scans refer to A-scans of this particular region of the eye fundus. The algorithm will be calibrated on this type of image; therefore, SCP images are the main scope of this proposal, eliminating the need to retrieve inner retinal slab or DCP scans.

Despite the widespread application of OCT in ophthalmology, particularly in diagnosing a broad range of retinal pathologies, the precise and objective delineation of specific retinal structures, such as the FAZ, remains a significant challenge. One of the main limitations is the lack of standardized guidelines for FAZ segmentation, which introduces inconsistencies in analysis and reduces diagnostic reliability. This issue extends beyond image processing concerns, as FAZ segmentation plays a crucial role in the early detection and monitoring of various ocular diseases, including diabetes mellitus and its retinal complications, and glaucoma. Currently, FAZ segmentation is predominantly performed manually by expert clinicians, a process that is time-consuming and subject to interobserver variability. Furthermore, the absence of a universally accepted segmentation protocol hinders repeatability and adds a subjective component to diagnostic assessments.

Several computational approaches have been proposed for OCT-based FAZ segmentation, ranging from edge-detection filters to morphological operations. For instance, in a study carried out by Schottenhamml et al. [2], the segmentation process is based on identifying the vessels surrounding the FAZ. Another approach, based on the method presented by Jia et al. [3], employs a decorrelation algorithm, which enhances the swept-source OCT technique by reducing phase-induced noise. Alternative methods also exist, one of which uses a shape that is gradually modified [4]. A minimal area of one pixel is first initialized in the centre of the image, which is progressively augmented until a boundary on the intensity levels is found.

Recent advancements have introduced deep learning techniques to enhance the accuracy and efficiency of FAZ segmentation. For example, Heisler et al. developed a deep neural network for single-zone automatic quantification of FAZ parameters and perifoveal vessel density [5]. Similarly, Díaz et al. proposed a fully automatic system combining image processing techniques to identify and segment the whole FAZ region precisely, achieving a high correlation with manual measurements [6]. Moreover, Wang et al. introduced a deep learning-based quality assessment and segmentation system, which processes OCTA images to assess quality and segment the FAZ area, facilitating clinical diagnosis and research [7].

Thus, in this context, we have recently presented a new segmented image database [8] along with a rigorous definition of the FAZ, which discerns between inner and external zones [9]. Building upon this framework, the present study aims to develop an automatic segmentation algorithm based on these criteria. The proposed method seeks to enhance segmentation accuracy and consistency, facilitating applications such as large-scale screening in at-risk populations and providing a reliable tool for clinical and research purposes.

2 | Methods

The main method used in the algorithm is convolution, which is a fundamental mathematical operation with wide-ranging applications in fields such as signal processing and machine learning. At its core, convolution involves the integration of two functions to produce a third function that characterizes how one of them interacts with the other as it is shifted and overlapped. This operation plays an important role in understanding and manipulating data across various domains. In our case, convolution is utilized to recognize the pattern of the vessels surrounding the FAZ. Given a function defined in a 2D space, labeled $f(x,y)$, and a convolutional kernel, labeled $g(x,y)$, the convolution $(f*g)(x,y)$ is defined as follows

$$(f*g)(x,y)=\int_{-\infty}^{\infty}\int_{-\infty}^{\infty} f(\tau_1,\tau_2)\, g(x-\tau_1,y-\tau_2)\,\mathrm{d}\tau_2\,\mathrm{d}\tau_1 \tag{1}$$

where $(*)$ denotes convolution. In the case of discrete functions (such as images, where the minimum step unit is a pixel), the integral is replaced by the sum over all pixels in the image. There are several properties associated with the convolution operation, such as the distributive property, which is particularly relevant and can be expressed as,

$$(f*g)(x,y)+(f*h)(x,y)=(f*(g+h))(x,y)=(f*u)(x,y) \tag{2}$$

This property allows for the composition of multiple kernels into a single mask, reducing the need to perform multiple convolutions separately. Another important property of convolution is commutativity,

$$(f*g)(x,y)=(g*f)(x,y) \tag{3}$$

In our case, convolution is used to detect the pattern depicted in the kernel across the OCTA image of the SCP. The result of the convolution of two images can be understood as the overlapping of the kernel $g(x,y)$ across the input image $f(x,y)$. That is, given an input image containing various patterns and a kernel depicting the particular pattern to be detected, the resulting convolution produces an output image where the desired feature appears with high intensity, while unwanted patterns are suppressed (Figure 1). Therefore, we need to adjust the kernel size to optimize the detection of specific structures.

In the first case, the most prominent feature in the output is the horizontal line, as it follows a pattern that matches the kernel (horizontal line), whereas the vertical line tends to blur and disappear. In the second case, where the kernel is rotated to detect vertical lines, the reverse occurs. Finally, in the third case, the kernel is a sum of the previous two, and the resulting image confirms the expected behavior according to the distributive property.

2.1 | Vascularity in the Fovea

Before proposing a segmentation algorithm, it is important to first describe the structural characteristics of the SCP. In general terms, the surrounding area of the fovea can be divided into two distinct regions: the vascularized area and the FAZ. However, as stated by our research group [9], the vascularized area is assumed to extend slightly beyond the visibly present blood vessels on the surface. This is due to the presence of capillaries in slightly deeper layers, which are not visible on the surface (although the presence of light spots can be appreciated, denoting the circulation of blood in these areas). This distinction allows us to divide the FAZ into two different sections, the transition

zone and the actual FAZ [9]. Nevertheless, the presence of these blood vessels in depth is not considered when segmenting the FAZ, resulting in predicted areas somewhat larger than the real ones. Some studies suggest using a combination of the SCP and DCP images of each patient to delineate the vascular-free zone [10]. In this article, we focus on the delineation of the FAZ using only superficial scans, as defined in [9], which is undoubtedly much simpler and faster in usual clinical practice.

For example, Figure 2a shows a lateral projection of the FAZ area. The central depression corresponds to the area strictly devoid of vascularity, referred to as the inner FAZ. Adjacent to this zone, underlying blood vessels within the deeper layers of the fovea are marked in red, producing a faintly illuminated area. This region is referred to as the extended FAZ or outer FAZ. Figure 2b shows a top projection of the SCP obtained by OCTA, highlighting two manually segmented distinct zones of the FAZ.

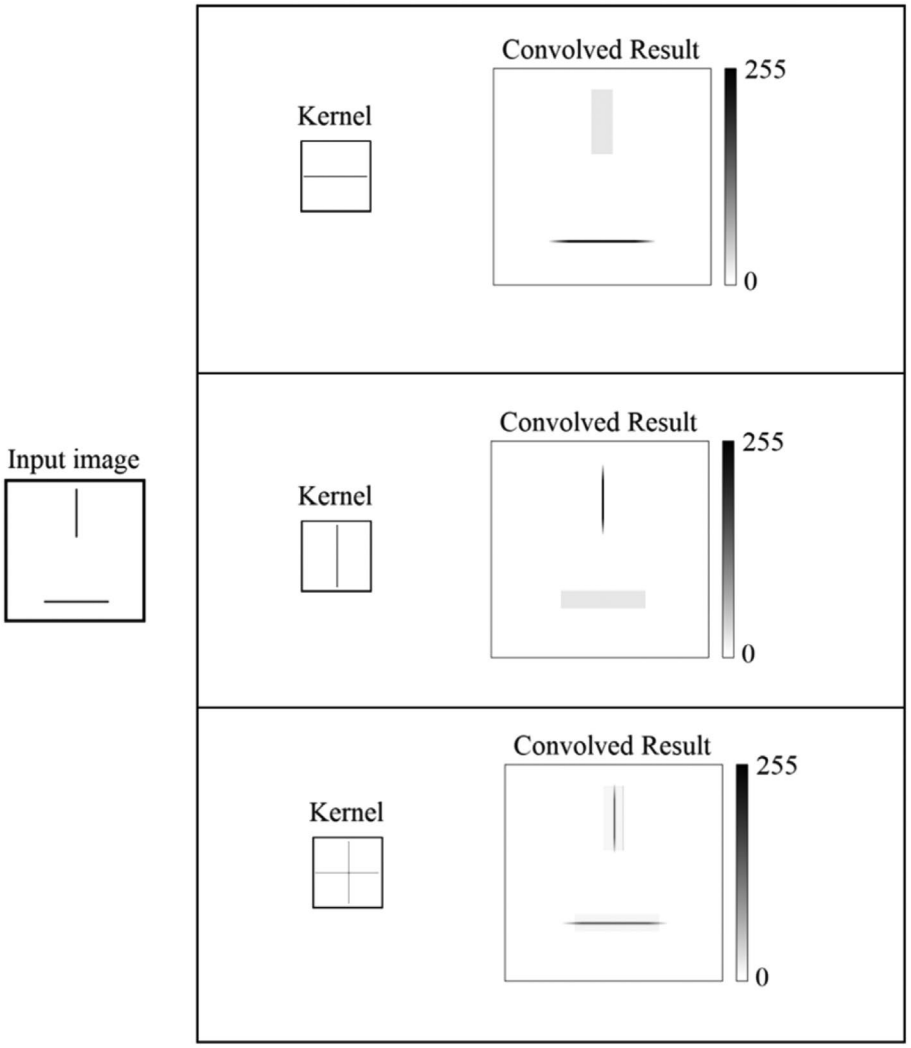

FIGURE 1 | Graphical representation of convolution and its distributive property. Applying different kernels over the same input image, we obtain three different results.

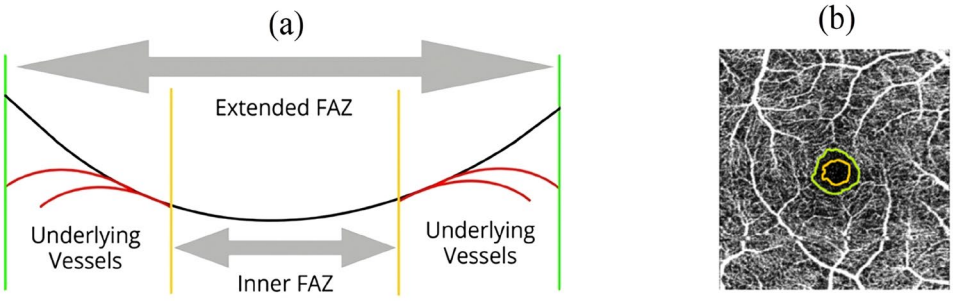

FIGURE 2 | (a) Schematic cross-section of the fovea. The yellow lines delimit non-vascularized zone (FAZ), and the green lines delimit the transition zone, where no vessels are observed on the surface, but vascularization is still present in layers below the surface. (b) Example of manual segmentation distinguishing the inner and extended FAZ.

With this understanding of the foveal structure, we turn our attention to the automatic segmentation process.

2.2 | Automatic Segmentation Algorithm

After these introductory notes, the workflow of the proposed FAZ segmentation algorithm can now be described. Our approach introduces a novel segmentation method based on the analysis of the bifurcations of the capillaries surrounding the FAZ. It is assumed that, on one hand, convolution detects the pattern present in the kernel across the input image, and on the other hand, that the sum of different convolutions can be condensed in a kernel with the sum of the different patterns in each one of the convolutions as stated in Equation (2).

A first proposed kernel consists of a simple blood vessel scheme that bifurcates into two branches. This is the pattern that is repeated throughout the image, making it a logical choice for the initial kernel design. However, pattern detection is dependent on the orientation of the kernel, meaning that in cases where the kernel is not rotation-invariant, only bifurcations aligned with the proposed direction will be detected. In this context, Figure 3 shows an example of a SCP image obtained by OCTA. In the vascularized region, blood vessels branch out, covering the entire area. Within the FAZ, no vessels or branching points are present. Nevertheless, as mentioned before, convolving the image with only one kernel does not produce satisfactory results due to direction dependence. Therefore, the image needs to be scanned with the kernel oriented in different directions. This process can be simplified by using the distributive property of convolution, as explained in (2), allowing multiple kernels to be merged into one. By combining the four kernels shown and smoothing the sharp edges with a Gaussian profile, the final kernel is obtained, as illustrated in Figure 3.

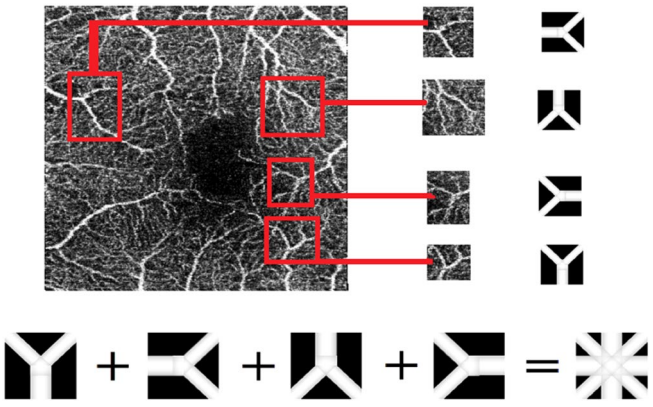

FIGURE 3 | Manual branching points detection in an OCTA image: A-scan of the Superficial Capillary Plexus (SCP) and matching filter for each case. Results of each convolution are also displayed below.

The basic automatic segmentation proposed in our code [11], is based on the process outlined in Figure 4. First, the input image is convolved with the proposed kernel, producing a probability map for branching points in all directions. Since the FAZ is a non-vascular zone, the lowest values on the probability map are expected to appear where the FAZ is located. By applying a threshold, the image is divided into two black and white areas; this is, a binarized mask is created that outlines the FAZ. This mask is then superimposed on the original image. To segment the extended FAZ, the same process applies, changing the threshold parameter. Key parameters to optimize in this process include mask size, kernel line width, and threshold level.

For this purpose, a dataset of 176 real OCTA images of the SCP was used. These 176 images correspond to 73 eyes from healthy subjects, 40 eyes from patients with type 1 Diabetes Mellitus (DM1) without visible signs of diabetic retinopathy, and 54 eyes from type 2 Diabetes Mellitus (DM2) patients with non-proliferative diabetic retinopathy (NPDR) without diabetic macular edema. DM2 patients with NPDR were diagnosed during the ophthalmology examination. The study was approved by the "Comité de Ética de la Investigación Clínica de la Comunidad de Aragón" (CEICA) with reference PI19/252 and complies with the principles of the Helsinki Declaration. Six scans where no clear FAZ is visible (Figure 5A) were discarded, in order to avoid calibration errors. The OCTA scans were performed using the DRI-Triton SS-OCT (Topcon Corporation, Tokyo, Japan). A 3×3mm macular three-dimensional scan was obtained, along with a 3×3mm OCTA scan, using IMAGEnet 6 software (Version 1.22.1.14101; Topcon Corporation, Tokyo, Japan).

In the design of new segmentation algorithms, it is common to compare the results with some other automatic method [12]. In our case we are unable to implement such a comparison, since there is no other method based on our definitions of FAZ. Therefore, we have had to do a statistical process based on manual segmentations. Thus, for each image in the dataset, six manual segmentations were performed by different experts, as Figure 5B shows. Computing the mean path of the six manual segmentations, we obtain a standard segmentation of each FAZ. We repeat the process with each image for the inner FAZ as well as for the outer border.

For each image, a mask containing the standard manual segmentation is obtained adding the six manually segmented areas. Then we obtain a final mask with values between 0 and 6. Values larger than 3 are marked as white, and the rest of the pixels in

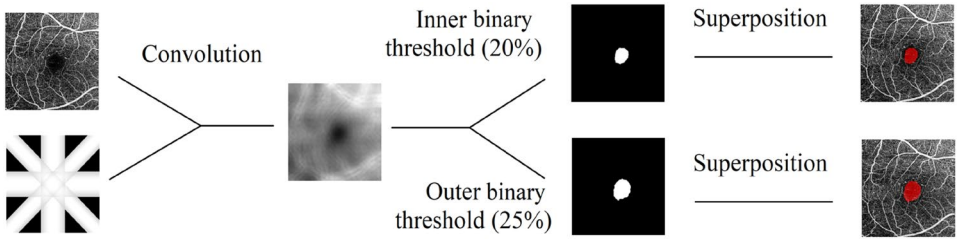

FIGURE 4 | Scheme depicting the basic segmentation algorithm [11]. It is necessary to define a kernel to proceed with the segmentation.

black. This process has been carried out for both inner and outer areas. Then, the automatic segmentation is performed, and the error is defined as

$$\epsilon = \frac{100 \times |I_{auto} - I_{manual}|}{N_x N_y \times 255} \quad (4)$$

where I_{auto} and I_{manual} are the binarized masks with the areas segmented by the algorithm and the average of the manual segmentations respectively. N_x and N_y are the pixel lengths (height and width) of the image ($N_x = N_y = 320$ pixels in our case), and 255 is the maximum intensity level, (thus, each white pixel counts as 1). Finally, the result is multiplied by 100, so it represents a percentage. Such error function yields 0% if the automated mask and the manual one match pixel-by pixel and 100% in the case the resultant mask is the negative of the manual one.

For the calibration process, the dataset was checked, and six images with no apparent FAZ, such as those shown in Figure 5A were excluded, so segmentation errors on those images were avoided. Subsequently, each of the remaining 170 images was segmented using different parameter combinations to determine the set of values yielding the lowest accumulated error, which was then established as the standard configuration. The objective of this iterative analysis was to calibrate three parameters in the algorithm: kernel size, kernel line width, and binarization threshold. For each image, the kernel size varied from 5 to 100 pixels in increments of 5, the line width was adjusted from 10% to 90% of the total kernel width in increments of 5%, and the binarization threshold was tested from 0.05 to 0.95 (5% to 95%) in increments of 0.05. This process resulted in a total of 6460 possible parameter sets, from which the one minimizing the average error was selected. The optimization process converged to the following set of parameters: a kernel size of 45 pixels, a line width of 8 pixels, and a threshold value dependent on the FAZ region under analysis. To differentiate between the inner and outer FAZ, the algorithm was applied using two distinct threshold values (one for each region). By performing two thresholding operations, two binary masks per image were generated. The final calibrated threshold values were 0.2 for the inner FAZ segmentation and 0.25 for the outer FAZ segmentation. These optimized settings are employed throughout the remainder of this study.

Once the final set of parameters was defined, the error was computed for the inner and outer segmentations, and a histogram for those values was generated, as shown in Figure 6. The error is computed in comparison to the manual segmentations used for calibration. Therefore, the presented errors do not relate to any automated segmentation method since there is no automatic method of segmentation using our new criteria.

It is observed that some cases exhibited errors greater than 2%, reaching a maximum of 3.5%. Although these errors were not excessive, they corresponded to scans in which there was limited agreement among manual segmentations. While these cases could have been excluded, they were retained to enhance the robustness of the algorithm.

The assessment of FAZ segmentation accuracy using manual segmentations as a reference has not been previously reported

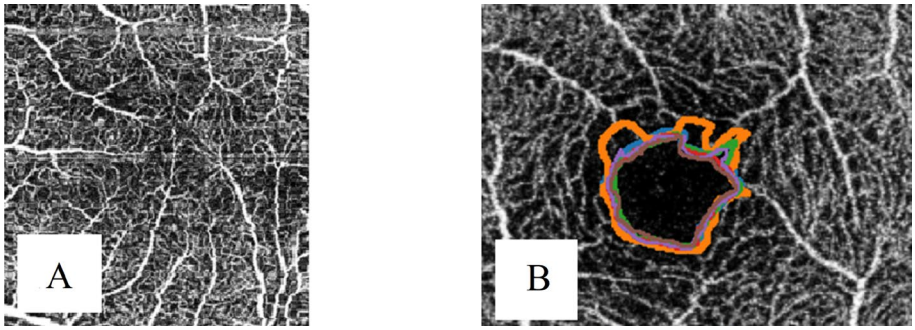

FIGURE 5 | (A) Example of an OCTA image (A-scan) of the Superficial Capillary Plexus (SCP) with no apparent Foveal Avascular Zone (FAZ). (B) Six manual segmentations of the external FAZ in one image. Both images are taken from [9].

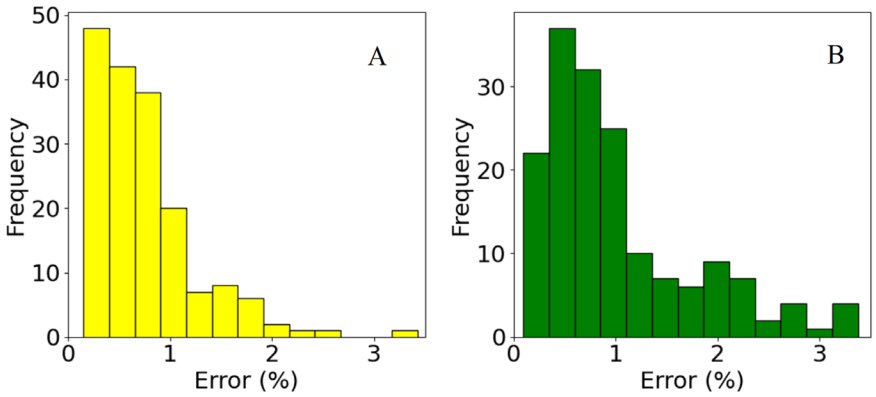

FIGURE 6 | Errors obtained from all segmentations. (A) Inner FAZ segmentation. (B) External FAZ segmentation.

in other algorithm validations. The use of a ground truth dataset provides a reliable standard for evaluating segmentation precision, allowing for a more accurate assessment of the performance of the algorithm [13–16]. To facilitate the reproducibility of this study, both the image database used and the developed code are made available to interested readers [11].

3 | Results and Discussion

As a first application of the algorithm, data and statistics were extracted from the automatic segmentations, trying to identify potential differences between patient groups. First, the images set used for software calibration were split into three groups, that is, Healthy subjects (H) (87 images), patients with DM1 (58 images), and patients with DM2 (25 images). Then, the error for each group was calculated according to Equation (4), using both the inner and outer FAZ definitions, and was plotted in the histograms presented in Figure 7.

It can be observed that the average error in the inner FAZ is generally smaller for DM1 and healthy subjects. In contrast, the histogram for the DM2 group is noticeably wider, with a mean error nearly twice that of DM1 patients. This may be attributed to the fact that the FAZ in DM2 patients tends to be more irregular, leading to greater variability among manual observers. While healthy subjects exhibit less variation in the inner FAZ, larger errors are observed in the outer FAZ segmentation.

Next, the relationship between the inner and outer FAZ was examined. First, the ratio between the inner and outer areas as a function of the inner area is shown in Figure 8a. It can be observed that, for larger values of inner area, the outer/inner area ratio tends to a stationary value around 1.25 (a reasonable result given that the outer threshold is set as 1.25 times the inner threshold). However, for smaller areas the ratio increases asymptotically as the inner FAZ area approaches a minimum. Thus, a large ratio (>3) may indicate a wrong inner FAZ segmentation, while lower values can be related to successful segmentations. Figure 8a also shows the different ratio obtained for each group of patients, revealing that the DM2 group presents more cases that deviate from the general trend. This can be explained by samples where the transition zone has a relatively larger area compared to its inner region, which may serve as an indicator for the detection of diabetic retinopathy.

To consider it from a different perspective, in Figure 8b the outer area is shown instead of the ratio. Since the outer FAZ is calculated using the same method as the inner FAZ, a linear trend is naturally observed. However, there are instances that diverge from this trend, with these deviations being more pronounced in the DM2 group. This serves as a further indication of potential abnormalities in the blood flow within the transitional area on DM2 patients.

Regarding the measured area values, it is noteworthy that DM2 and healthy subjects show inner areas greater than $0.3\,mm^2$, which does not occur in the DM1 group. Given the high percentage of patients in other groups and the number of scans for each group, it cannot be discarded that DM1 patients present a smaller FAZ.

In addition, in Figure 8a, for smaller inner area values, the ratio tends to increase. This phenomenon occurs because, as the inner area approaches zero, the surrounding area (the external area of the outer FAZ) remains nearly constant. Consequently, as the inner area decreases, the quotient becomes larger.

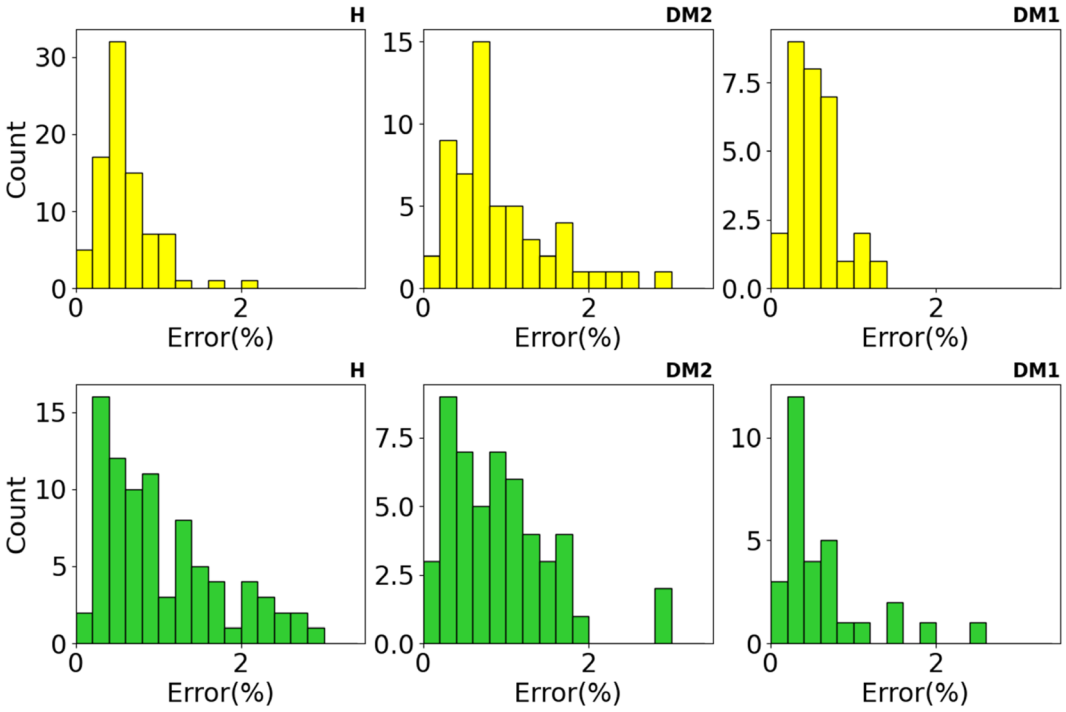

FIGURE 7 | Histogram depicting the errors obtained in the different series. Yellow graphs correspond to inner FAZ segmentations, while the green ones correspond to external FAZ segmentations. DM1: Type 1 Diabetes Mellitus patients without diabetic retinopathy. DM2: Type 2 Diabetes Mellitus patients with non-proliferative diabetic retinopathy without diabetic macular edema. H: healthy group.

Next, the acircularity index is studied. Acircularity is a metric designed to further analyze the contour shape. While perimeter and area provide size-related information, acircularity analyzes the shape of the boundary comparing it to a perfect circle. Given a closed contour formed by a set of points, acircularity is defined as

$$Acircularity = \frac{\sigma(r)}{< r >}$$

where "r" is the set of radial coordinates of the contour points, measured from the mass center of the enclosed area. The results obtained from analyzing all the contours by patient groups are shown in Figure 9a. The outer perimeter progression in regard to inner perimeter is also shown in Figure 9b, where probably, the reduced number of atypical values is related to the low acircularity of the contours (<0.2). Further examination of Figure 9a reveals that the DM2 group exhibits a higher deviation from the average value compared to the other groups. Specifically, the inner and outer FAZ acircularity values remain below 0.2 and 0.1, respectively, in most cases, which is a noteworthy finding. Although the FAZ generally exhibits a circular shape, cases with acircularity below 0.1 are rare, indicating that the FAZ is not perfectly circular in any group or size. Figure 9b further supports this observation, as it demonstrates that the outer perimeter follows a linear trend relative to the inner perimeter, suggesting a similar shape for both inner and outer areas. However, DM2 patients exhibit a more irregular FAZ morphology, as evidenced by the greater dispersion around the linear fit compared to the other groups.

Finally, the axis ratio can also be graphed. To obtain this measurement, the contour is expressed in polar coordinates, and then fitted to the equation of an ellipse, where the free parameters are both axes. Comparing the axis ratio value between the outer and inner contours, the results presented in Figure 10 are obtained.

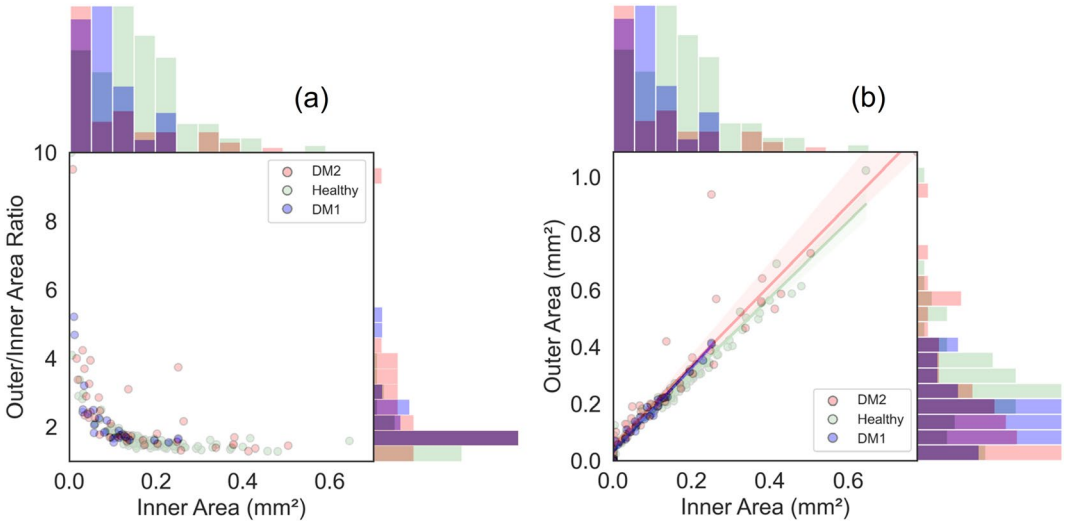

FIGURE 8 | (a) Evolution of the area ratio as a function of the inner area size. (b) Comparison of outer and inner area values. Again, the lower areas of the DM1 measurements of the patients can be observed, as well as the higher dispersion for the DM2 group measurements.

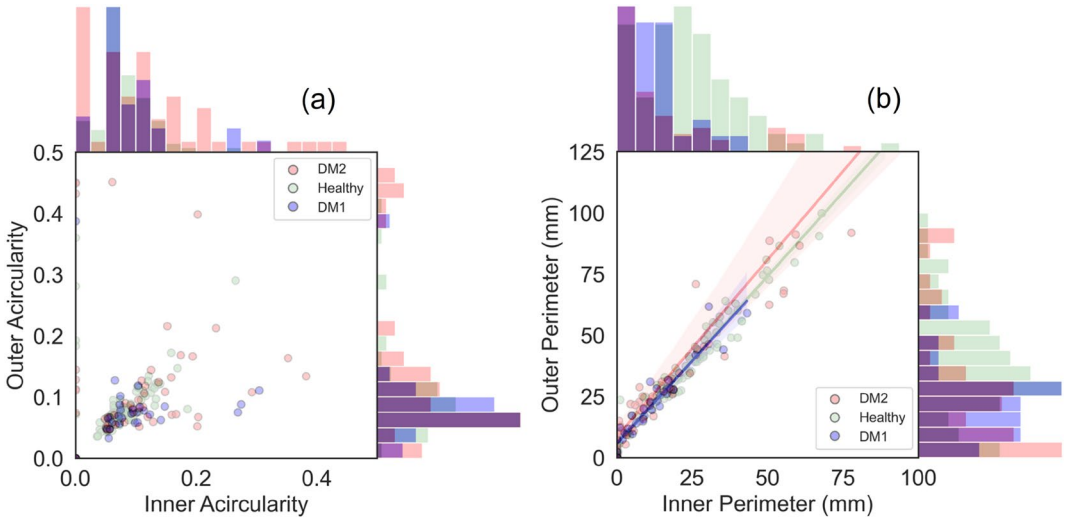

FIGURE 9 | (a) Inner versus Outer acircularity measurements. It is observed that, for DM1 patients, outer acircularity tends to be lower than in the other groups. (b) Outer versus inner perimeter. The results obtained are very similar to those of the areas, but with less atypical values. Again, the DM2 group shows much higher dispersion than the other groups.

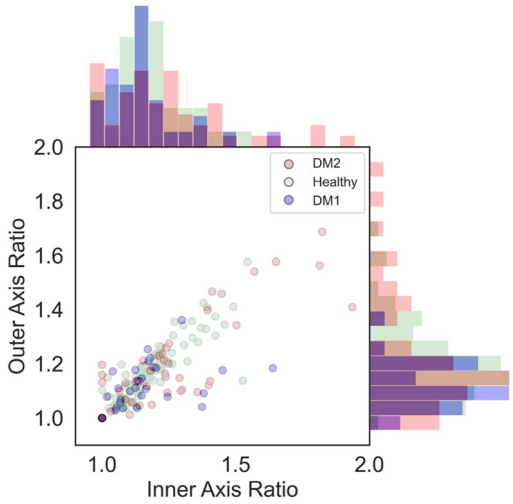

FIGURE 10 | Comparison of axis ratio for outer and inner contours. It can be observed that the DM1 group shows more circular FAZ areas (as the ratios are closer to 1). The grid in this graph also proves all values are over 1.

In addition to reaffirming that DM1 patients tend to exhibit more circular FAZ shapes (if the axis ratio is closer to 1, the length of the axes is similar, so the ellipse tends to be a circle), an upward linear trend is observed. So, inner FAZ areas with high axis ratios tend to correspond to outer FAZ areas with similarly high axis ratios, and vice versa. Another notable observation, resulting from the low acircularity values, is the limited number of axis ratio values exceeding 1.3, as both parameters are interrelated.

Regarding both areas and perimeters, DM1 patients tend to present lower values, indicating that this group presents a smaller FAZ area in both inner and outer regions compared to the other groups. Another pattern observed among the different graphs is that, while DM1 patients present lower areas in general, DM2 patients exhibit greater variability. This suggests a higher irregularity in the presented data, which could be attributed to a less standardized FAZ shape among the group. In other words, DM2 patients may present a wider range of FAZ shapes compared to the other groups, potentially reflecting slight shape distortions in these individuals.

4 | Conclusions

The development and refinement of image processing techniques, particularly in the field of ophthalmology, have increased our ability to diagnose ocular illnesses. OCT technology has emerged as an important tool for capturing detailed images of the eye fundus, particularly of the fovea, which is critical for monitoring retinal health. Despite the advancements in OCT, challenges persist, particularly in the objective delineation of the FAZ in the different retinal vascular plexuses. The absence of standardized guidelines and the reliance on manual segmentations introduce variability and subjectivity into diagnostic assessments. Various approaches, including those employing convolution algorithms, have been explored to address this challenge.

In this context, we proposed a novel algorithm for FAZ segmentation in the SCP OCTA images [11], based on recent research on unified FAZ manual segmentation methods [9]. Our algorithm, based on convolution, aims to detect branching points on the surrounding vessels to segment the FAZ instead of analyzing the vasculature itself. To do so, a new kernel is introduced, based on three parameters: kernel size, line width, and thresholding percentage, which are then calibrated to minimize errors across all 170 images. This method offers repeatability and performance improvements over other solutions without the need for costly computational methods. By adopting this new segmentation approach, we aim to mitigate the variability inherent in single-segmentation methods due to the increased information provided. Not only do we propose the new algorithm workflow, but we also provide the full ready-to-use code, as well as all the images used for calibration and testing purposes as a complementary dataset.

Through a calibration and validation process, we demonstrated the efficacy of our algorithm in accurately segmenting the FAZ and transition zone. The algorithm offers three adjustable parameters: kernel size (measured in pixels), line width (as a percentage of the total kernel size), and thresholding. The kernel size ranges from 5 to 100 in increments of 5, while the line width percentage also ranges from 0% to 100% of the total kernel width, with 5% intervals. Certain impractical values, such as extreme thresholds or a 0%-line width, are excluded to optimize the calibration process. From the 6460 valid parameter combinations, the one that minimizes the average error is selected. Specifically, the optimal parameters are 45 pixels for kernel size, 20% of line width (8 pixels), and a 20% thresholding level for the inner FAZ and 25% for the outer FAZ.

Once the calibration process is completed, the results obtained from the automatic segmentation are analyzed. Our analysis of segmented areas revealed distinct patterns across patient groups, particularly in diabetic retinopathy cases, showing the potential for clinical applications. We observed that in all the area and perimeter measurements, patients in the DM1 group tend to present lower area values. For the other groups, the inner FAZ area ranges from 0.05 to 0.5 mm^2, while in the DM1 group, no values over 0.25 mm^2 are observed. In addition, the DM2 group displayed greater dispersion in the measurements, with the linear fitting dispersion being noticeably larger in the DM2 group than in the other two, despite the DM2 group having half the number of samples.

Another result worth mentioning is that inner and outer FAZ areas tend to be proportional. For a large FAZ (understanding as large FAZ the one that shows an inner FAZ larger than the difference between inner and outer FAZ), it has been shown that the outer area is approximately 30% larger than the inner, which can be used as a measurement of FAZ standardization. In fact, images that show a substantially different ratio than the one mentioned tend to depict smaller FAZ areas, which may be indicative of DM1 patients, or distorted shapes, which could suggest DM2 patients. Apart from these results, both the code developed, and the collection of images used have been made publicly available.

While the proposed algorithm demonstrates clear advantages in terms of segmentation accuracy and repeatability, it is important to acknowledge some limitations. For instance, although the performance of the algorithm was tested across a variety of images, the generalizability to more diverse populations with different stages of retinal pathology remains uncertain. As it

has been stated, the calibration of the algorithm was based on manual segmentation performed by six experts, but it does not imply that the segmentations constitute a ground truth or a perfect benchmark, but rather a simple guideline to start working with. Therefore, neither is the algorithm completely free of errors, nor can we ensure that it will work correctly on any image since its behavior will depend on the quality of the scans, apart from possible errors in the six manual segmentations used in the calibration process. In this sense, Hassan et al. [17] reviewed, for example, automatic models for retinal disease screening. They acknowledged challenges like generalizability across diverse populations and integration into clinical workflows. Thus, further testing on larger, more heterogeneous datasets would help to validate the robustness and reliability of our algorithm. Additionally, while the calibration parameters were optimized for the current dataset, it is also possible that other parameter configurations might yield improved results for specific patient groups or imaging conditions. Future work will focus on enhancing the algorithm's adaptability to a wider range of OCTA images, including those affected by more advanced stages of diabetic retinopathy with diabetic macular edema, or any other retinal condition. Furthermore, integrating this algorithm into clinical workflows may require additional considerations, such as compatibility with different OCT devices or the need for manual verification in cases where segmentation results deviate significantly from expected patterns. Despite these considerations, the presented algorithm offers a promising tool for the automated analysis of OCTA images, potentially improving diagnostic accuracy and efficiency in ophthalmology.

Funding

The authors have nothing to report.

Ethics Statement

The study was approved by the "Comité de Ética de la Investigación Clínica de la Comunidad de Aragón" (CEICA) with reference PI19/252 and complies with the principles of Helsinki.

Conflicts of Interest

The authors declare no conflicts of interest.

Data Availability Statement

The data that support the findings of this study are available from the corresponding author upon reasonable request.

References

1. T. E. de Carlo, A. Romano, N. K. Waheed, and J. S. Duker, "A Review of Optical Coherence Tomography Angiography (OCTA)," *International Journal of Retina and Vitreous* 1 (2015): 5, https://doi.org/10.1186/s40942-015-0005-8.

2. J. Schottenhamml, E. M. Moult, S. Ploner, et al., "An Automatic, Intercapillary Area-Based Algorithm for Quantifying Diabetes-Related Capillary Dropout Using Optical Coherence Tomography Angiography," *Retina* 36, no. 1 (2016): S93–S101, https://doi.org/10.1097/IAE.0000000000001288.

3. Y. Jia, O. Tan, J. Tokayer, et al., "Split-Spectrum Amplitude-Decorrelation Angiography With Optical Coherence Tomography," *Optics Express* 20 (2012): 4710–4725, https://doi.org/10.1364/OE.20.004710.

4. Y. Lu, J. M. Simonett, J. Wang, et al., "Evaluation of Automatically Quantified Foveal Avascular Zone Metrics for Diagnosis of Diabetic Retinopathy Using Optical Coherence Tomography Angiography," *Investigative Ophthalmology & Visual Science* 59, no. 6 (2018): 2212.

5. M. Heisler, F. Chan, Z. Mammo, et al., "Deep Learning Vessel Segmentation and Quantification of the Foveal Avascular Zone Using Commercial and Prototype OCT-A Platforms," 2019.

6. M. Díaz, J. Novo, P. Cutrín, F. Gómez-Ulla, M. G. Penedo, and M. Ortega, "Automatic Segmentation of the Foveal Avascular Zone in Ophthalmological OCT-A Images," *PLoS One* 14, no. 2 (2019): e0212364.

7. Y. Wang, Y. Shen, M. Yuan, et al., "A Deep Learning-Based Quality Assessment and Segmentation System With a Large-Scale Benchmark Dataset for Optical Coherence Tomographic Angiography Image," 2021.

8. F. J. Salgado Remacha, I. Pinilla, and C. Ruiz-Tabuenca, "Manual OCT-A FAZ Segmentation for MD1, MD2, and Healthy Patients: Zenodo," 2025.

9. G. Fernández-Espinosa, C. Ruiz-Tabuenca, E. Orduna-Hospital, I. Pinilla, and F. J. Salgado-Remacha, "A Reliable Criterion for the Correct Delimitation of the Foveal Avascular Zone in Diabetic Patients," *Journal of Personalized Medicine* 12, no. 5 (2023): 822, https://doi.org/10.3390/jpm13050822.

10. C. Lavia, S. Bonnin, M. Maule, A. Erginay, R. Tadayoni, and A. Gaudric, "Vessel Density of Superficial, Intermediate, and Deep Capillary Plexuses Using Optical Coherence Tomography Angiography," *Retina* 39, no. 2 (2019): 247–258, https://doi.org/10.1097/IAE.0000000000002413.

11. SegmentFAZ, "OCT-A Scanning Utility for FAZ Segmentation and Further Analysis," https://github.com/CRuizHUB/SegmentFAZ.

12. L. Kreitner, J. C. Paetzold, N. Rauch, et al., "Synthetic Optical Coherence Tomography Angiographs for Detailed Retinal Vessel Segmentation Without Human Annotations," *IEEE Transactions on Medical Imaging* 43, no. 6 (2024): 2061–2073, https://doi.org/10.1109/TMI.2024.3354408.

13. R. Linderman, A. E. Salmon, M. Strampe, M. Russillo, J. Khan, and J. Carroll, "Assessing the Accuracy of Foveal Avascular Zone Measurements Using Optical Coherence Tomography Angiography: Segmentation and Scaling," *Translational Vision Science & Technology* 6, no. 3 (2017): 16, https://doi.org/10.1167/tvst.6.3.16.

14. R. E. Linderman, M. N. Muthiah, S. B. Omoba, et al., "Variability of Foveal Avascular Zone Metrics Derived From Optical Coherence Tomography Angiography Images," *Translational Vision Science & Technology* 7, no. 5 (2018): 20.

15. N. Eladawi, M. Elmogy, F. Khalifa, et al., "Early Diabetic Retinopathy Diagnosis Based on Local Retinal Blood Vessel Analysis in Optical Coherence Tomography Angiography (OCTA) Images," *Medical Physics* 45, no. 10 (2018): 4582–4599, https://doi.org/10.1002/mp.13142.

16. F. Coscas, A. Sellam, A. Glacet-Bernard, et al., "Normative Data for Vascular Density in Superficial and Deep Capillary Plexuses of Healthy Adults Assessed by Optical Coherence Tomography Angiography," *Investigative Ophthalmology & Visual Science* 57, no. 9 (2016): 211–223, https://doi.org/10.1167/iovs.15-18793.

17. B. Hassan, H. Raja, T. Hassan, et al., "A Comprehensive Review of Artificial Intelligence Models for Screening Major Retinal Diseases," *Artificial Intelligence Review* 57 (2024): 111, https://doi.org/10.1007/s10462-024-10736-z.